

# Investigating the effects of bulk supercooling and rapid solidification on Co–Ni–Ga ferromagnetic shape memory alloys

Haamun Kalaantari · Shaahin Amini ·  
Jeongmin Hong · Reza Abbaschian

Received: 2 December 2010 / Accepted: 9 April 2011 / Published online: 26 April 2011  
© Springer Science+Business Media, LLC 2011

**Abstract** In this study, Electromagnetic Levitation (EML) technique was utilized to explore the effect of bulk supercooling and rapid solidification in alloys with  $\text{Co}_{46}\text{Ni}_{27}\text{Ga}_{27}$  and  $\text{Co}_{48}\text{Ni}_{22}\text{Ga}_{30}$  (at.%) compositions. The effects of  $\gamma + \beta$  on the martensitic and austenitic transformation temperatures and magnetic properties were investigated. The presence of  $\gamma$  phase was found to suppress the martensitic and austenitic transformations to below room temperature. Bulk supercooling and rapid solidification led to the formation of homogeneous martensitic phase from the hyperperitectic  $\text{Co}_{46}\text{Ni}_{27}\text{Ga}_{27}$  alloy. In contrast with pure martensite phase in  $\text{Co}_{48}\text{Ni}_{22}\text{Ga}_{30}$ , the hyperperitectic martensite in supercooled  $\text{Co}_{46}\text{Ni}_{27}\text{Ga}_{27}$  sample showed no grain boundaries microsegregation and embrittlement that caused deep cracks along grain boundaries. The sample had a high Curie temperature about 400 K and good directional magnetic properties.

## Introduction

A new class of smart materials called Ferromagnetic Shape Memory Alloy (FSMA) in a Ni–Mn–Ga ternary system was discovered in 1996 [1]. Since then, it has been observed that FSMA materials with a *Heusler-type* structure possess both ferromagnetic and shape memory behavior, with a large reversible strain up to 6% in a

particular crystallographic direction under an applied magnetic field [2]. These properties make the materials promising candidates for Micro-Electro-Mechanical-Systems (MEMS) and aerospace applications, such as sensing and actuating devices [3]. Alloy systems exhibiting such Ferromagnetic Shape Memory (FSM) behavior cover variety of alloys including Fe–Pd [4], Fe–Pt [5], Ni–Mn–Ga [1, 6–8], Co–Ni–Al [9–12], and Co–Ni–Ga [9, 13–16].

The Co–Ni–Al and Co–Ni–Ga FSMA were recently found to exhibit better ductility compared to other FSMA because of the dispersion of ductile phase ( $\gamma$ ) in  $\beta'$  (martensite form of  $\beta$ ) matrix at certain compositions [9, 16–18]. The improvement in ductility of FSMA is a desirable characteristic for subsequent processing steps and ultimate device fabrication. In addition, the Co–Ni–Ga FSMA also possess relatively high Curie and martensitic transformation temperatures [9, 16].

The FSM behavior in Co–Ni–Ga alloy is reported to be restricted to those compositions which have a single  $\beta$ -phase with B2 structure (bcc-ordered structure) [9, 16] since  $\beta$  can undergo a martensitic transformation, contributing to shape memory behavior [9, 14, 17].  $\beta$ -Phase in the binary Co–Ga and Ni–Ga systems have compositions ranging from 30 to 66.7 and 31.3 to 60 at.% Ga, respectively (Fig. 1a) [19]. In contrast, the Co–Ni alloys form a solid–solution ( $\alpha\text{Co},\text{Ni}$ ) with A1 structure (fcc-disordered structure) and exhibit ferromagnetic behavior at all compositions, and their magnetic transformation temperatures decrease with increasing nickel content [20]. The magnetic transformation temperature of the ternary alloy also decreases as nickel content increases. This has been reported by Oikawa [9, 16] who showed that the magnetic and martensitic transformations of ternary Co–Ni–Ga alloys can be adjusted by varying Cobalt–Nickel ratio. Craciunescu et al. [14] also showed an increasing

H. Kalaantari (✉) · S. Amini · R. Abbaschian  
Department of Mechanical Engineering, University  
of California, Riverside, CA 92521, USA  
e-mail: haamunk@engr.ucr.edu

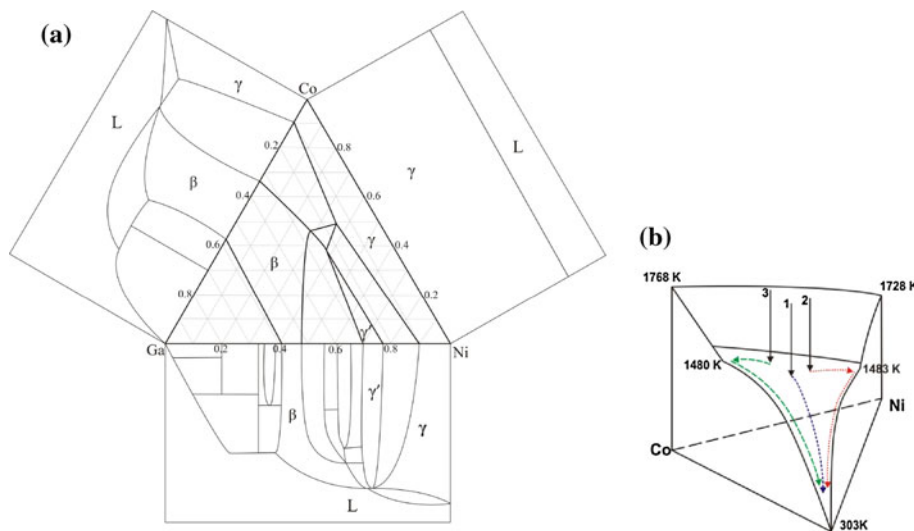
J. Hong  
Department of Electrical Engineering, University of California,  
Riverside, CA 92521, USA

martensitic transformations ( $M_s$ ) temperature with increasing average valence electron concentration (electron/atom ratio or e/a). Similar observations have been made by other researchers for  $\text{Ni}_2\text{MnGa}$  alloys [21, 22].

Conventional processing of the alloys frequently leads to microsegregation and grain boundary embrittlement. This is mostly because  $\beta$  phase has a narrow composition range which decreases with decreasing temperature. The single-phase  $\beta$  region projected from the binary diagrams is shown in Fig. 1a [19, 23]. The region represents the dual phase  $\gamma + \beta$  composition in the vicinity of  $\text{Co}_{50}\text{Ni}_{25}\text{Ga}_{25}$  (at.%) ( $\text{Co}_2\text{NiGa}$ ), known as *Heusler-type*,  $\text{L}2_1$  structure above its martensitic transformation temperature. This crystal structure would transform to a tetragonal and/or orthorhombic martensitic structure [15, 16].

In general, the solidification route of a ternary alloy could be predicted if the liquidus surface contour of the ternary phase diagram is known. The liquidus surface contour of a Co–Ni–Ga alloy (Fig. 1b) can be visualized using the binary diagrams. There are three possible paths for conventional solidification depending on the curvature of the surface contour and composition, as schematically shown in the figure. One path, although less likely, would lead directly to the formation of a Ga-rich liquid at the end of solidification, while the two others lead toward Ni or Co-rich regions first then toward the Ga-rich liquid. Because of one or the other of these solidification paths, conventional solidification techniques of the alloy cannot only lead to severe chemical segregation but also grain boundary embrittlement. Such microsegregation and nonhomogeneity strongly influence the martensitic transformation. As such, it is generally necessary to homogenize the alloy, which requires long time and high temperatures.

**Fig. 1** **a** A  $\beta$ -phase region and two-phase area in Co–Ni–Ga ternary system at room temperature projected from binary diagrams [19, 23], and **b** three possible solidification routes; toward (1) Ga-rich, (2) Ni-rich, and/or (3) Co-rich regimes for Co–Ni–Ga alloys with compositions in the  $\beta$ -phase region



It has been recognized that bulk supercooling before solidification can lead to rapid solidification process (RSP) which in turn to partitionless (massive) solidification [24]. Such a large bulk supercooling can be achieved using various techniques such as glass fluxing, emulsification, or levitation [25]. Electromagnetic levitation (EML) melting is more conducive for achieving high supercooling in high temperature alloys because of its containerless nature. The technique also allows direct observation and measurement the specimen's temperature. Furthermore, as described elsewhere, the EML can be complemented with a copper chilling device, to rapidly solidify the supercooled liquid.

In this research, the solidification of  $\text{Co}_{46}\text{Ni}_{27}\text{Ga}_{27}$  (at.%), centered around *Heusler-type* composition, and a non-stoichiometric Co–Ni–Ga alloy with  $\text{Co}_{48}\text{Ni}_{22}\text{Ga}_{30}$  (at.%) composition was investigated using EML.

## Experimental procedure

Co–Ni–Ga specimens of approximately  $1.5 \pm 0.05$  g each with compositions of  $\text{Co}_{46}\text{Ni}_{27}\text{Ga}_{27}$  and  $\text{Co}_{48}\text{Ni}_{22}\text{Ga}_{30}$  (at.%) were prepared from high purity Co (99.99%), Ni (99.99%), and Ga (99.999%) by arc-melting in Ar (99.99%) environment. To achieve homogeneity, each sample was molten twice with the specimen being turned over before the second melting. The arc-melted samples were then levitated in the EML apparatus, as per the procedure reported in [24–26]. The levitation system consisted of a double wound in opposite directions coil [27] which was powered by a 20-kW high-frequency (8 MHz) generator, an inert gas delivery system connected to a gas purifier, and a temperature-measuring device equipped with a data-acquisition system. A quartz tube with 16-mm

diameter and 0.5-mm thickness was inserted inside the coil to provide a protective Argon gas environment for the levitated sample. To control the temperature of the levitated sample, helium was added to gas stream to increase the heat removal and cooling when needed. Both argon and helium gases were purified using a gas purifier with a titanium getter at 800 °C.

A two-color pyrometer was employed to measure the temperature of the sample continuously. The accuracy of the pyrometer readings was checked by measuring the melting temperature of pure nickel and pure copper, as well as selected binary Ni–C and Fe–C binary alloys. It was found that for these samples the measured temperatures were within  $\pm 10$  °C of the expected values with small oscillations due to sample rotation and vibration, as well as liquid circulation. Based on computed velocity and temperature fields for a 6-mm-levitated iron droplet proposed by El-Kaddah et al. [28], a severe circulation is expected within the sample as well. The fluid flow field in levitated metal droplets only can be driven by two forces, i.e., electromagnetic force and the buoyancy force fields. This topic is far beyond the scope of this article, but the computational analysis of the temperature and flow fields in the levitated droplet can be found in [28]. This vigorous circulation causes a uniform temperature distribution with a maximum 7 °C difference from surface to core of droplet.

The as-solidified specimens were etched using a solution consisting of HCl, CH<sub>3</sub>COOH (Glacial), HNO<sub>3</sub>, and water. The microstructures were observed using an optical and scanning electron microscopy. The chemical composition of  $\gamma$  and  $\beta$  phases were determined by energy dispersive spectroscopy (EDS) system at 20 kV using a standard “ZAF” (Z-atomic number, A-absorption, and F-fluorescence, plus background and dead time corrections) technique. The Curie temperature  $T_C$  and the magnetization  $M$  were measured using a vibrating sample magnetometer (VSM). The martensitic and austenitic transformation temperatures were determined by a differential scanning

calorimeter (DSC) at cooling and heating rates of 1 and 10 °C/min, respectively.

## Results and discussion

### Microstructures

To investigate the effects of rapid solidification on microstructure and phase evolution, two different compositions Co<sub>46</sub>Ni<sub>27</sub>Ga<sub>27</sub> (at.%) and Co<sub>48</sub>Ni<sub>22</sub>Ga<sub>30</sub> (at.%) were solidified under different conditions. For the first alloy, specimens of approximately 7-mm diameter were levitated and solidified with three different conditions: (i) rapid quenching of superheated melt against a copper chill, (ii) superheating and slow cooling in the levitation state using helium gas, and (iii) bulk supercooling and rapid quenching against the copper. The Co<sub>48</sub>Ni<sub>22</sub>Ga<sub>30</sub> (at.%) specimen was also levitated and solidified with superheating and rapid solidification. The processing conditions and nominal composition of the alloys are given in Table 1. The table also shows the liquidus temperature and the temperature at which the levitated samples were dropped.

The cross-sectional microstructures of a sample with Co<sub>48</sub>Ni<sub>22</sub>Ga<sub>30</sub> (at.%) composition at a location near the copper chill are shown in Fig. 2a. The figure shows martensite laths within the grains whose boundaries are decorated with a Co-rich phase. The SEM examination of the sample, Fig. 2b, showed deep cracks along grain boundaries of martensitic matrix phase. The spot EDS analysis on the wall of a removed grain revealed high amounts of Ni and Co at the boundary. Although exact compositional determination could not be made because of the relatively large beam diameter of EDS, the approximate chemical composition at the boundary surface was determined as 52%Co–36%Ni–12%Ga. The  $\beta'$  martensite phase had an average composition close to the nominal composition of the alloy (parental phase).

**Table 1** Nominal composition and condition of alloys in this study

Sample	Composition (at.%)	Melting temperature (°C)	Dropping temperature (°C)	Quenching	Observed microstructure
D1	Co <sub>48</sub> Ni <sub>22</sub> Ga <sub>30</sub>	$T_{\text{liquidus}} = 1210$ Superheating at $T_{\text{S.H.}} = 1326$	$T_{\text{drop}} = 1326$	Dropped on Cu-chill (brittle)	Single phase
C2	Co <sub>46</sub> Ni <sub>27</sub> Ga <sub>27</sub>	$T_{\text{liquidus}} = 1254$ Superheating at $T_{\text{S.H.}} = 1400$	$T_{\text{drop}} = 1400$	Dropped on Cu-chill	Dual phases
C6	Co <sub>46</sub> Ni <sub>27</sub> Ga <sub>27</sub>	$T_{\text{liquidus}} = 1240$	$T_{\text{drop}} \approx 1000$ (solid)	Cooled during levitation	Dual phases
C11	Co <sub>46</sub> Ni <sub>27</sub> Ga <sub>27</sub>	$T_{\text{liquidus}} = 1265$ Supercooled at $T_{\text{S.C.}} = 1122$ ( $\Delta T = 143$ )	$T_{\text{drop}} = 1122$	Dropped on Cu-chill	Single +Dual phases (two zones)

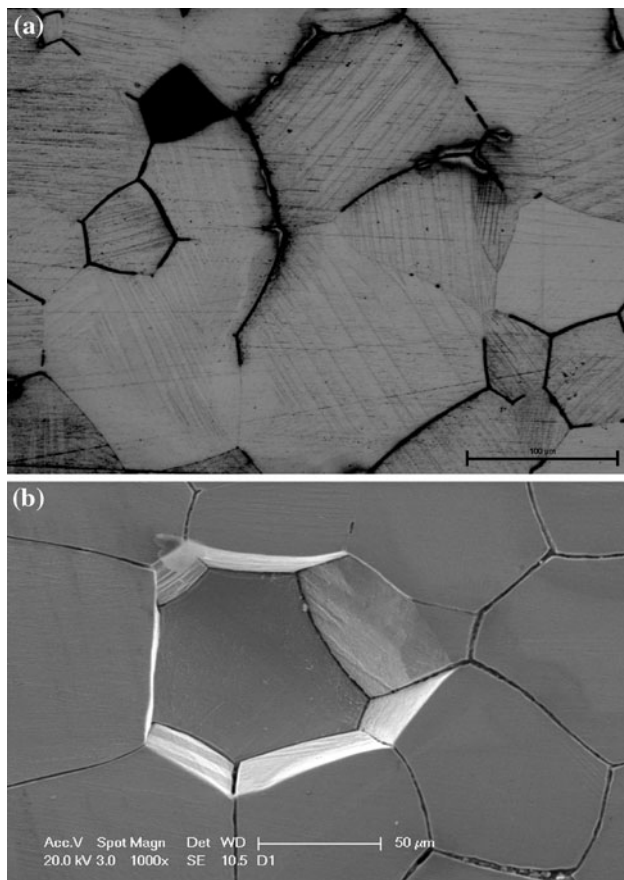


**Fig. 2** **a** Microstructures of a  $\text{Co}_{48}\text{Ni}_{22}\text{Ga}_{30}$  (at.%) sample quenched from superheated melt. The grain boundaries contain cobalt-rich phase. **b** SEM micrograph (sample D1) shows severe grain boundaries embrittlement that caused detached grains and one fallen-off grain

The microstructure of the superheated and quenched  $\text{Co}_{46}\text{Ni}_{27}\text{Ga}_{27}$  (at.%) sample, Fig. 3a, consisted of primary  $\gamma$  dendrites embedded in  $\beta$  matrix. It can be seen that some of the defragmented  $\gamma$  dendrites form curved bands because melt shearing flow by electromagnetic stirring. The core of the dendrites had composition of 53%Co–26%Ni–21%Ga whereas the  $\beta$  phase just surrounding the dendrite tip (dark area in Fig. 3b) had a composition of 42%Co–28.5%Ni–29.5%Ga. The microstructure and measurements are indicative of the peritectic transformation for the alloy, similar to the one shown in the quasi-binary diagram in Fig. 4. Away from this peritectic interface, the martensite matrix had an average composition of 43%Co–28%Ni–29%Ga. Other studies have also shown that Co–Ni–Ga alloys with composition near to Heusler-alloy solidify through a peritectic reaction,  $\text{L} + \gamma \rightarrow \beta$  [29, 30]. In Fig. 4, a pseudo binary diagram for  $\text{Co} \approx 47$  at.% in terms of Ga content has been used for showing the peritectic reaction [31]. The microstructure of another  $\text{Co}_{46}\text{Ni}_{27}\text{Ga}_{27}$  sample with the same composition as the previous sample (sample C6), but cooled slowly, was also found to consist

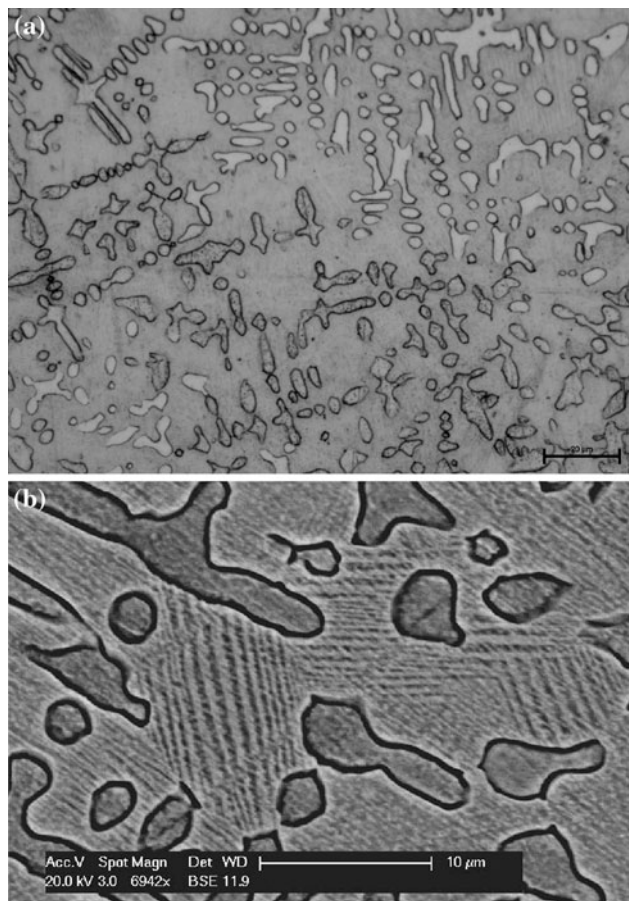


**Fig. 3** **a** Dendritic microstructure of primary  $\gamma$  phase of  $\text{Co}_{46}\text{Ni}_{27}\text{Ga}_{27}$  (at.%) sample quenched from the superheated melt. **b** BSE micrograph (sample C2); martensite matrix is shown

of primary  $\gamma$  dendrite embedded in martensite matrix, as shown in Fig. 5. The dendritic  $\gamma$  phase had a core composition of 55%Co–24%Ni–21%Ga with the martensitic matrix with average composition of 44%Co–27%Ni–29%Ga.

Figure 6 shows the microstructure of a  $\text{Co}_{46}\text{Ni}_{27}\text{Ga}_{27}$  alloy which was supercooled by 143 °C before being quenched against the copper chill. This sample, which had a disk shape, consisted of two distinct microstructures as shown in the figure. The region next to the chill consisted of 100% martensitic structure. The second region, away from the chilled surface, consisted of  $\gamma$  dendrites surrounded by martensite. The martensite in the first region (zone I), designated as “off-composition martensite,” has formed from metastable  $\beta$  phase. It had a composition of 46%Co–27%Ni–27%Ga, similar to the parent alloy. The two-phase area far from the quenched surface(zone II), on the other hand, contained  $\gamma$  dendrite of 54%Co–25%Ni–21%Ga and martensite with 43%Co–29%Ni–28%Ga composition. In contrast with sample D1 shown in Fig. 2a, no cracks or intergranular precipitations were observed in

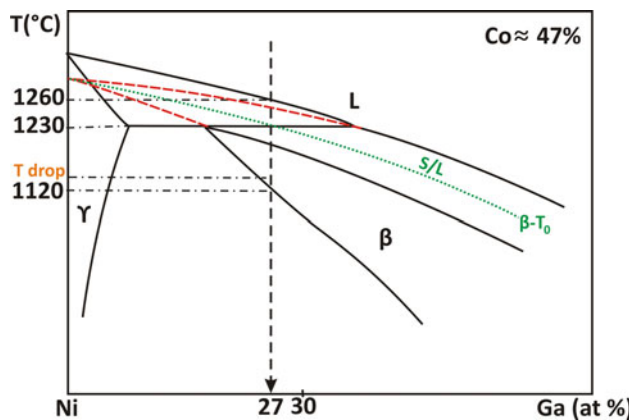


**Fig. 4** A pseudo binary diagram for Co–Ni–Ga alloys containing 47 at.% Co [28]. The metastable extension of the liquidus and solidus lines and  $T_0$  line for the  $\beta$  phase are also shown. The dashed arrow shows the composition of the supercooled sample as described in the text

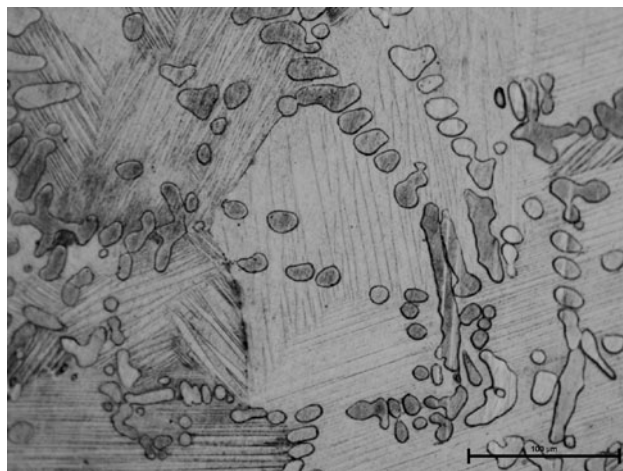


**Fig. 5** Microstructure of  $\text{Co}_{46}\text{Ni}_{27}\text{Ga}_{27}$  (at.%) sample slowly cooled during levitation (sample C6), consisting of fragmented dendrites and interdendritic martensite matrix

zone I. The zone II microstructure was similar to those in Figs. 3 and 5, but at a much finer scale.

The off-composition martensitic phase formation in the zone I indicates the influence of supercooling and rapid solidification on the microstructure. This can be surmised with the aid of metastable extension of the liquidus and solidus line for  $\beta$  and  $T_0$  curve, as shown in Fig. 4. When the supercooled contacts copper chill, the first solid nucleates and forms at a temperature designated by  $T_{\text{drop}}$ . Since this temperature is below the  $T_0$  for  $\beta$ , it will form without partitioning, and will have the same composition as the parent phase. As recalescence raises the temperature above Peritectic and  $\beta$ -L  $T_0$ , partitioning then takes place with the liquid solidified, the same way as those in Figs. 3 and 5.

It should be noted that, beside the formation of metastable composition, the supercooling also strongly

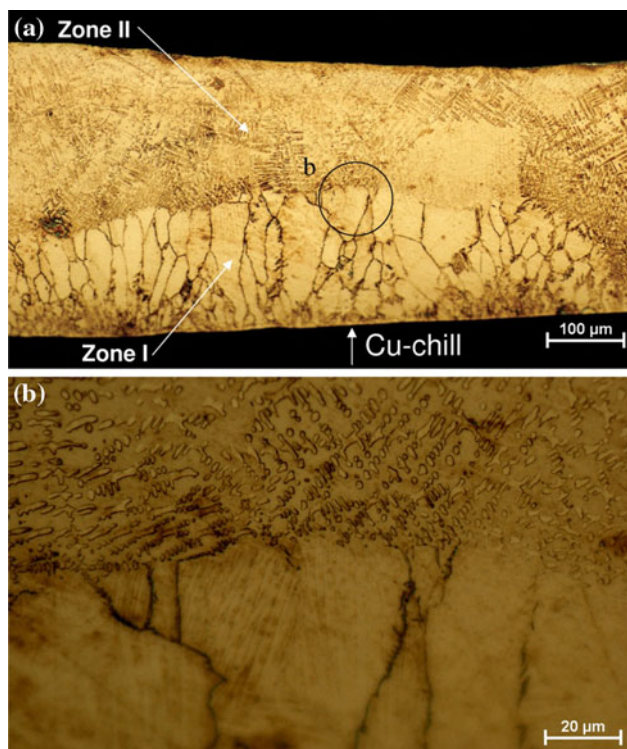


**Fig. 6** Microstructure of  $\text{Co}_{46}\text{Ni}_{27}\text{Ga}_{27}$  (at.%) sample solidified with  $\Delta T = 143$  °C supercooling (sample C11). **a** The lower portion (zone I), solidified near the chill surface, consists of non-equilibrium, off-composition martensite. The upper portion (zone II) contains primary  $\gamma$  dendrite and interdendritic  $\beta'$  (martensitic  $\beta$ ). **b** A higher magnification of interface between two different zones

increases the interface velocity. It has been shown that as the interface velocity increases, the partitioning coefficient ( $k_v$ ) becomes large and approaches unity with complete solute entrapment [32–36]. The influence of supercooling on the interface velocity can be described considering the thermal condition at a moving solid–liquid (S/L) as given by the Stefan's equation:

$$v_i = \frac{K_{S,i}G_{S,i} - K_{L,i}G_{L,i}}{\rho_S H_f} \quad (1)$$

where  $K_{S,i}$  and  $K_{L,i}$  are the thermal conductivities on the solid and liquid sides at the interface,  $\rho_S$  is the density of solid,  $H_f$  is the heat of fusion of solids and  $G_{S,i}$  and  $G_{L,i}$  are the temperature gradients at the interface on the solid and liquid side, respectively. For the supercooled liquid, the  $G_{L,i}$  term is negative, and it enhances the interface velocity. However, as solidification proceeds, the heat of recalescence alters the magnitude of the temperature gradients on both sides of the interface and consequently reduces the interface velocity. In addition, the recalescence could raise the liquid temperature above  $T_0$ , where partitioning (segregation) takes place. To prevent the recalescence above  $T_0$  for a supercooled melt, the supercooling needed is approximately  $\Delta T = \frac{H_f}{C_{P,L}}$ , where  $C_{P,L}$  is the heat capacity of

the liquid. Another approach would be to combine supercooling with rapid heat removal by quenching against a conductive substrate, which is the case for this study.

It is believed that solute entrapment or partitionless solidification of the supercooled sample shown in Fig. 6 has led to the formation of the single  $\beta$  phase from the hyperperitectic alloy. Subsequently, the  $\beta$ (BCC) has transformed to the off-composition  $\beta'$ (BCT). As such, the composition of martensitic phase ( $\beta'$ ) is the same as that of the parent liquid.

### Martensitic transformation

The DSC curves for sample D1 are shown in Fig. 7a and b, respectively, for two different heating/cooling rates of 10 and 1 °C/min. Exothermic and endothermic peaks are observed during cooling and heating cycles, respectively, in Fig. 7a. These peaks correspond to the martensitic and reverse transformations for the alloy at 10 °C/min cooling/heating rate. The austenite and martensite phase transformation temperatures ( $A_s$  for austenite starting transformation,  $A_f$  for austenite finishing,  $M_s$  for martensite starting, and  $M_f$  for martensite finishing), were determined by the point of intersection of the tangent line of the peak's inclination and baseline in the DSC curves. The values were 60, 95, 37.5, and 6 °C, respectively for the first heating/cooling cycle. A small downward shifts of the martensitic transformation temperatures ( $M_s$  and  $M_f$ ), about 5 °C for each cycle, were observed during subsequent cooling cycles. The reverse transformation to austenite ( $A_s$  and  $A_f$ ) also shifted downward but with a much larger degree. For example,  $A_s$  changed from 60 to 50, 42, and eventually to 30.5 °C between the first and fourth cycles.

The DSC curves of the same sample as above but at a slower heating/cooling rate of 1 °C/min are shown in Fig. 7b. During the first heating cycle, the reverse martensite transformation peak was observed near the same temperatures as in the first cycle of the curves shown in Fig. 7a. However, no martensitic transformation was observed during the cooling cycle even though the sample was cooled to -15 °C. The subsequent cycles were also devoid of martensitic or austenitic transformations. The comparison of the two DSC curves may indicate decomposition and/or change of austenite composition during the slow heating process (1 °C/min). Such compositional and phase change could conceivably suppress the martensite transformation temperature to well below -15 °C. A similar influence of heat treatment on the martensitic transformation temperature has been reported by other investigators for both heat-treated single-phase  $\beta$  (B2-type) and a single crystal of Co<sub>48</sub>Ni<sub>22</sub>Ga<sub>30</sub> alloy [16, 29]. It should be noted that two other peaks are also observed in Fig. 7b around 180 °C during heating and cooling of this

sample. These peaks are believed to indicate the Curie temperature ( $T_C$ ) of the sample.

The typical DSC curve for sample C2 is shown in Fig. 8a. In contrast with the sample shown in Fig. 7a, pronounced exothermic martensitic and endothermic austenite transformation peaks around 30–60 °C are not observed in this sample. However, there are small peaks in cooling and heating cycles that, respectively, show  $M_s$  and  $A_f$  to be around -21 and -4 °C. It should be noted that these transformation temperatures are below those reported in Ref. [31] for the same alloy composition. The difference in these two observations is believed to be because the sample in this study consisted of two phases, where as those of the previous studies were for the heat-treated single phase.

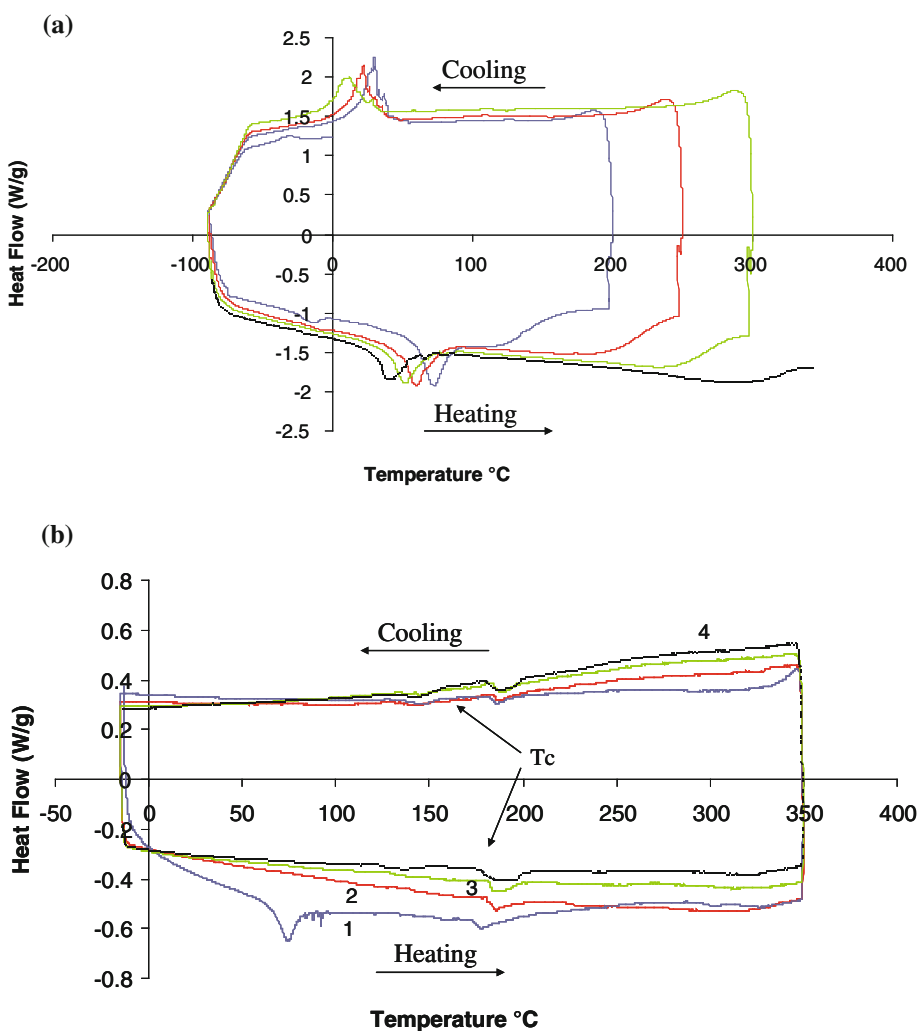
Similarly, Fig. 8b shows the DSC curve for sample C6, which consisted of two phases,  $\gamma$  and  $\beta$ . The  $M_s$  and  $A_f$  temperatures during the first cycle were around -20 and -2 °C, respectively. However, for the latter sample, the peaks are more pronounced since the martensite matrix has higher percentage in comparison with sample C2.

The DSC curves for sample C11 are shown in Fig. 8c, where both endothermic and exothermic peaks in the first cycle can be seen. Martensitic starting and reverse finishing transformation temperatures,  $M_s$  and  $A_f$ , are -15 and -6 °C, respectively. Although the  $M_s$  temperature has increased by about 6 °C, the martensitic and reverse transformations temperatures are still suppressed to temperatures quite below room temperature due to the presence of  $\gamma$ (dendrite) +  $\beta'$  phases in this sample (zone II) along with pure martensite microstructure,  $\beta'$  (zone I). As the heating and cooling cycles continued to higher temperature ranges, these two peaks become weak and finally disappear. The other broad peak around 150 °C in the second heating cycle that may indicate some form of solid-state transformation. It is conceivable that this correlates with the decomposition of the off-composition phase in zone I.

### Magnetization

The magnetization hysteresis loops ( $M$  vs.  $H$ ) at different temperatures for the Co<sub>48</sub>Ni<sub>22</sub>Ga<sub>30</sub> (at.%)  $\beta$  single-phase alloy, sample D1, is shown in Fig. 9. The "in-plane" magnetization ( $\theta = 0^\circ$ ) in the figure refers to the plane of the sample which was parallel to the quenched surface, and the "out-of-plane" magnetization ( $\theta = 90^\circ$ ) refers to the direction perpendicular to the chill surface. The magnetic saturation for both in-plane and out-of-plane magnetization directions decreased from about 45 to 40 emu/g with increasing temperature from 65 to 150 K, and then fell to 32.6 emu/g at room temperature (295 K). Similarly, the coercive forces (inserted graphs in Fig. 9) decreased with increasing temperature from 50 Oe at 65 K to 10 Oe at

**Fig. 7** DSC graphs of four heating/cooling cycles for  $\text{Co}_{48}\text{Ni}_{22}\text{Ga}_{30}$  (at.%) sample quenched from the superheated melt (sample D1) with cooling/heating rates: **a** 10 °C/min and **b** 1 °C/min



room temperature for both in-plane and out-of-plane magnetization directions. The in-plane magnetization curves were found to be more easily saturated (at 5 kOe) than out-of-plane magnetization curves (at 10 kOe) at all temperatures.

For sample C2, the magnetic saturation for both in-plane and out-of-plane magnetization directions decreased from 52 to 48 emu/g with increasing temperature from 65 to 150 K, and dropped to 38 emu/g at room temperature. The coercive force for this sample also decreased with increasing temperature from 100 Oe at 100 K to 10 Oe at room temperature for in-plane magnetization direction, and from 75 Oe at 100 K to 10 Oe at room temperature for out-of-plane magnetization direction. Similarly, the magnetic saturation for both in-plane and out-of-plane magnetization directions of sample C6 decreased from 52 to near 48 emu/g with increasing temperature from 65 to 150 K, and then to 38.2 emu/g at room temperature. The coercive forces also decreased with increasing temperature from 25 Oe at 65 K to 5 Oe at room temperature for both in-plane and

out-of-plane magnetization directions. For sample C11, which was supercooled and quenched, the magnetic saturation for both in-plane and out-of-plane magnetization directions decreased from 52 to 48 emu/g with increasing temperature from 65 to 150 K, and reduced to 38 emu/g at room temperature. The coercive forces decreased with increasing temperature from 30 Oe at 65 K to 10 Oe at room temperature for in-plane magnetization direction and from 80 emu/g at 65 K to about 30 emu/g at room temperature for out-of-plane magnetization direction.

For comparison, Fig. 10 shows  $M-H$  curves for both in-plane and out-of-plane magnetization directions at room temperature for  $\text{Co}_{48}\text{Ni}_{22}\text{Ga}_{30}$  and  $\text{Co}_{46}\text{Ni}_{27}\text{Ga}_{27}$  samples (C2, C6 and C11). In Fig. 10a, the difference in magnetic moment of both in-plane and out-of-plane directions reflects the anisotropic texture and directional properties of purely martensitic phase of sample D1 at room temperature. It has been shown in Fig. 10b that the magnetic properties of sample C2 also changed through different orientations in the same way as mentioned earlier.

**Fig. 8** DSC graphs of four heating/cooling cycles with 10 °C/min heating/cooling rate of  $\text{Co}_{46}\text{Ni}_{27}\text{Ga}_{27}$  (at.%) samples  
**a** C2, **b** C6 and **c** C11 (with  $\Delta T = 143$  °C supercooling)

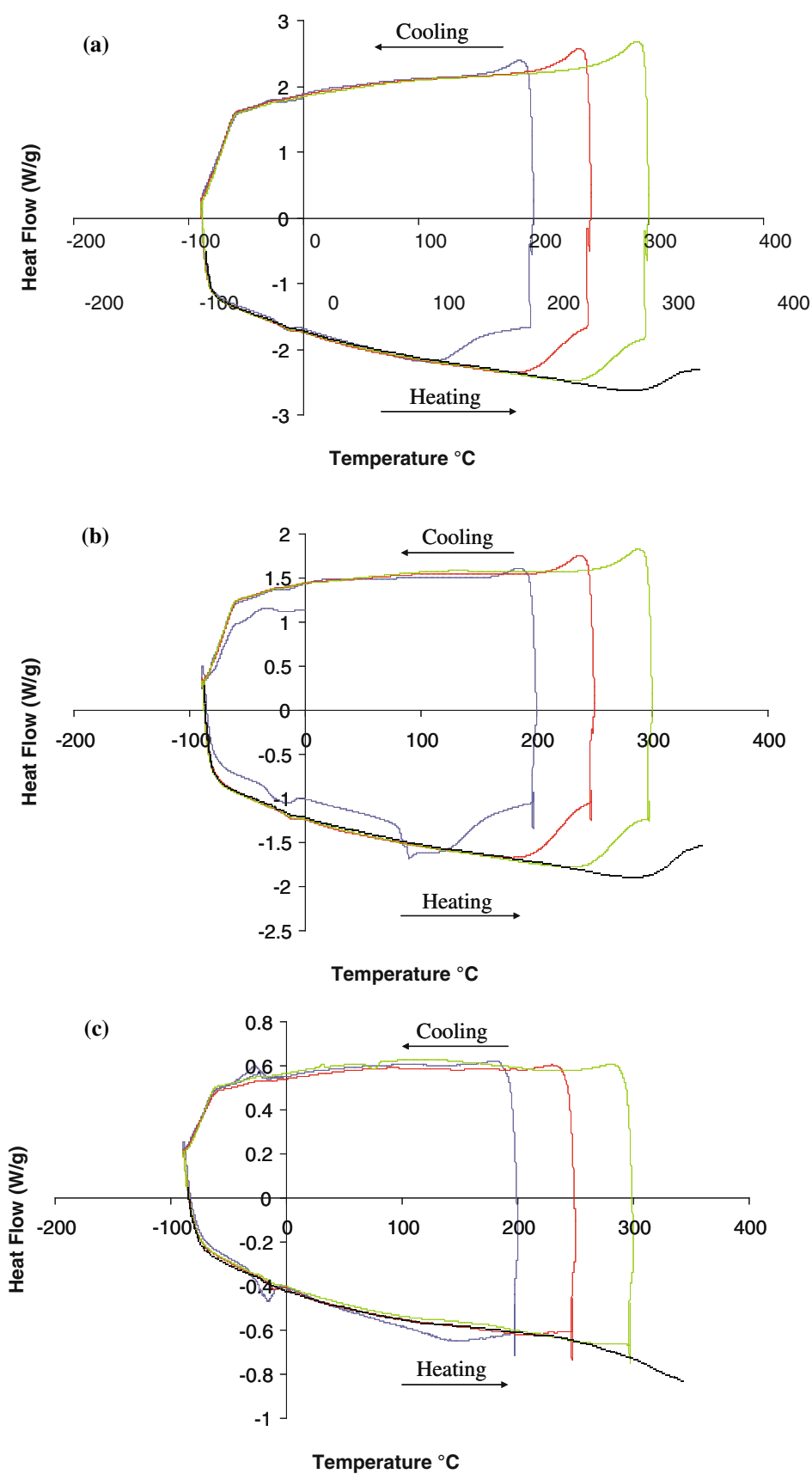


**Fig. 9** Magnetization ( $M$ ) curves in different temperature of  $\text{Co}_{48}\text{Ni}_{22}\text{Ga}_{30}$  (at.%) alloy quenched from the superheated melt (sample D1): **a** in-plane ( $\theta = 0^\circ$ ) and **b** out-of-plane ( $\theta = 90^\circ$ )

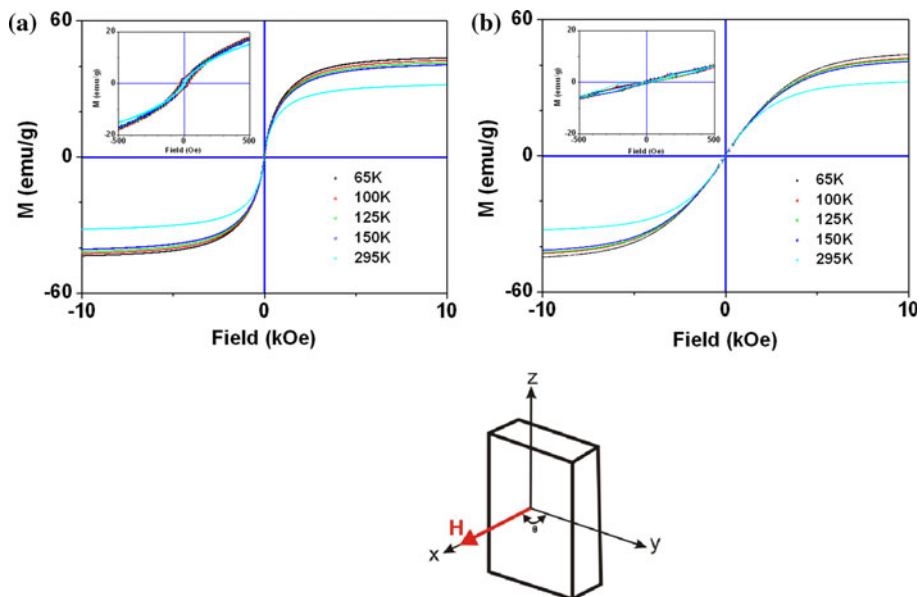
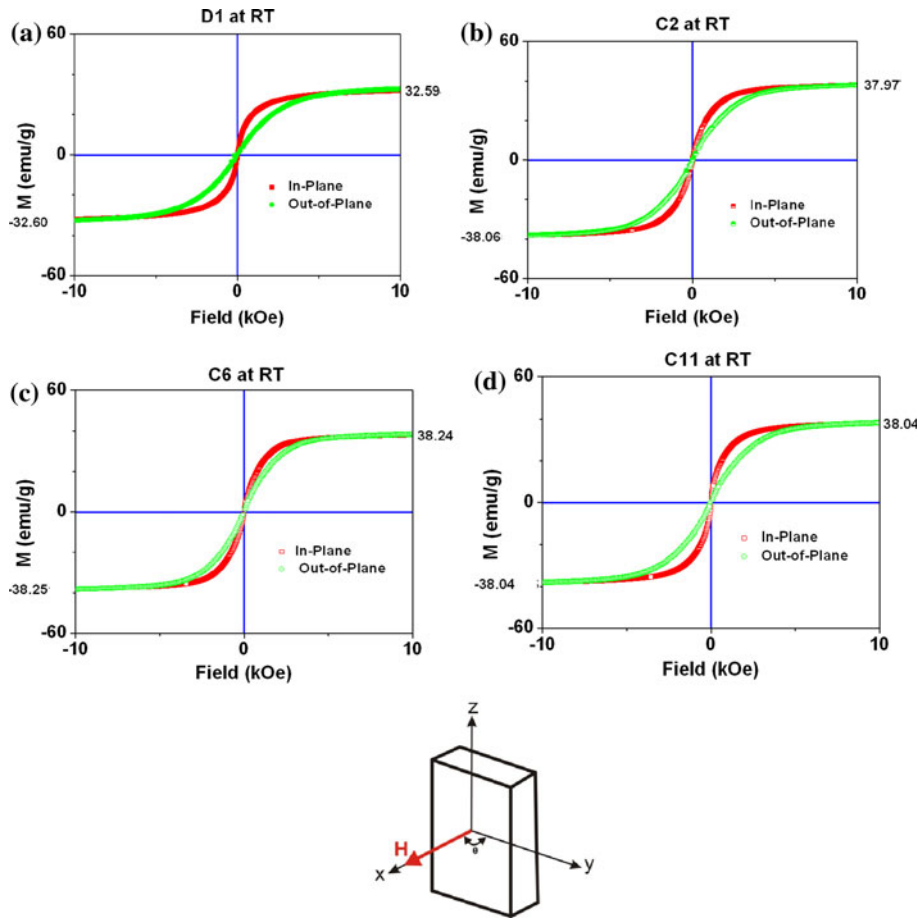


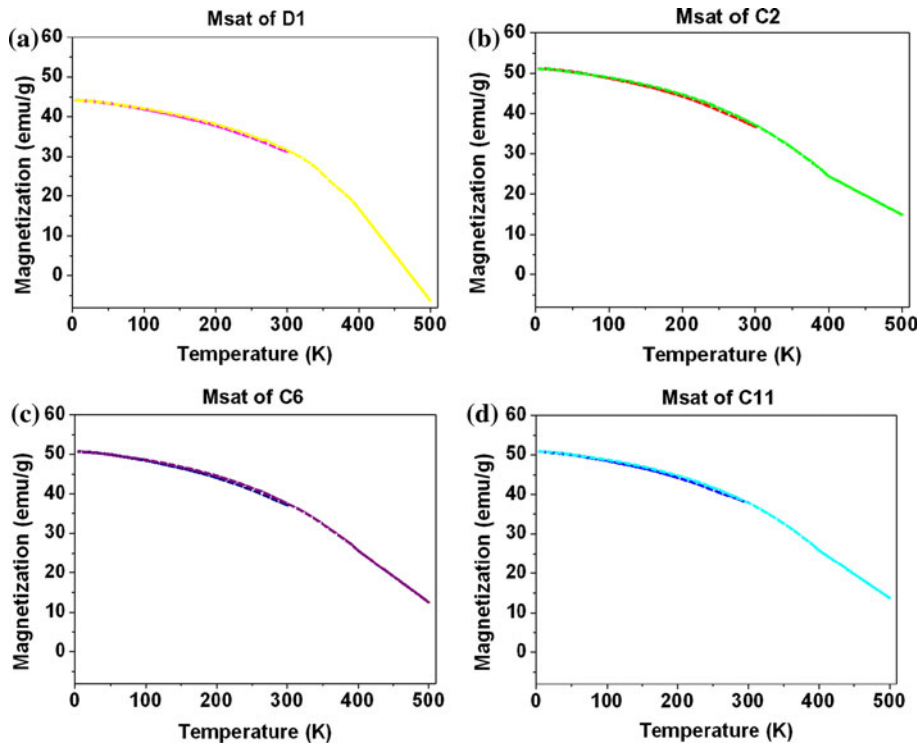
**Fig. 10**  $M$ - $H$  curves at room temperature of **a**  $\text{Co}_{48}\text{Ni}_{22}\text{Ga}_{30}$  (at.%) (sample D1), and  $\text{Co}_{46}\text{Ni}_{27}\text{Ga}_{27}$  (at.%) samples **b** C2, **c** C6, and **d** C11



However, the difference between magnetization curves in two main directions was less than the one in sample D1. The directional magnetic property decreased because of martensite matrix and  $\gamma$  ( $\beta' + \gamma$ ) phase forms instead of purely martensite phase of sample D1. The magnetic

saturation increased from 32.6 emu/g for sample D1 to 38 emu/g at room temperature in this sample owing to its near-Heusler composition. Magnetic moment of sample C6 (Fig. 10c) had different amounts along both directions. Nevertheless, the directional magnetic property in this

**Fig. 11** Saturation magnetization ( $M_{\text{sat}}$ ) in different temperatures (dashed and solid lines are related to cooling and heating cycles, respectively) of **a** Co<sub>48</sub>Ni<sub>22</sub>Ga<sub>30</sub> (at.%) (sample D1) and Co<sub>46</sub>Ni<sub>27</sub>Ga<sub>27</sub> (at.%) samples **b** C2, **c** C6, and **d** C11



sample had the lowest amount compared with other samples due to the formation of martensite matrix and  $\gamma$  ( $\beta'$  +  $\gamma$ ) phases, as well as different sample shapes from others (not completely flat). The saturation magnetization at room temperature had the same amount of sample C2 (38 emu/g).

For sample C11 in Fig. 10d, the magnetic properties also changed through different orientations as discussed earlier, but the difference is even higher than that of purely martensite phase in sample D1. The saturation magnetization of this sample at room temperatures also had higher amount (38 emu/g) than sample D1 (32.6 emu/g) because of its near-Heusler composition. Moreover, it is approximately equal to other Co<sub>46</sub>Ni<sub>27</sub>Ga<sub>27</sub> (at.%) samples regardless of their different microstructures (see Fig. 10).

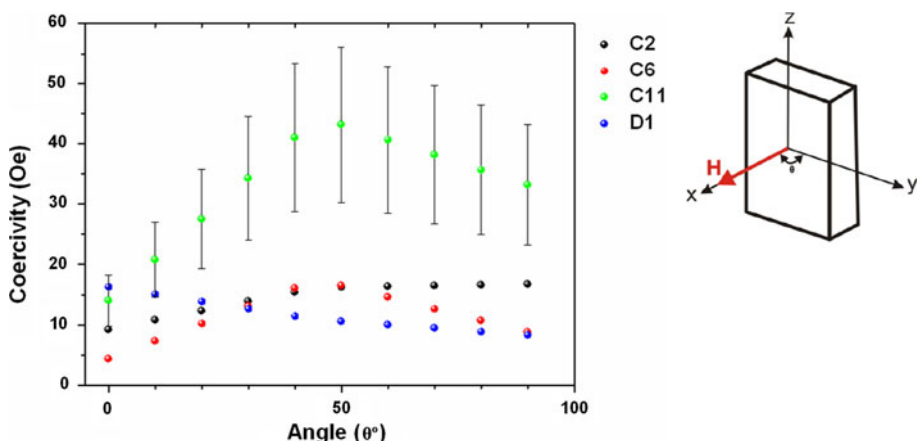
To investigate the Curie temperature, the saturation magnetization ( $M_{\text{sat}}$ ) at different temperatures for Co<sub>48</sub>Ni<sub>22</sub>Ga<sub>30</sub> (at.%) (sample D1) and Co<sub>46</sub>Ni<sub>27</sub>Ga<sub>27</sub> alloys (samples C2, C6, and C11) have been plotted in Fig. 11. All of Co<sub>46</sub>Ni<sub>27</sub>Ga<sub>27</sub> samples had well-above room temperature Curie temperatures around 400 K as a point of slope change in magnetization curves. However, this was not very accurate due to measurement limitations above 400 K. For Co<sub>48</sub>Ni<sub>22</sub>Ga<sub>30</sub> alloy (sample D1) as an off stoichiometric alloy of Heusler-type composition, the Curie temperature was about 350 K and was not sensitive to compositional changes. Figure 12 shows coercive force in different directions at room temperature for Co<sub>48</sub>Ni<sub>22</sub>Ga<sub>30</sub> (sample D1) and Co<sub>46</sub>Ni<sub>27</sub>Ga<sub>27</sub> samples (C2, C6, and C11). It has

been found that the supercooled and rapidly solidified Co<sub>46</sub>Ni<sub>27</sub>Ga<sub>27</sub> alloy (sample C11) had the highest directional coercivity among these samples. The minimum and maximum coercive forces were obtained around 14 Oe at  $\theta = 0^\circ$  and 45 Oe at  $\theta \approx 50^\circ$ , respectively. The coercive forces in samples C2, C6, and D1 were not dependent on the direction.

## Conclusion

Electromagnetic Levitation (EML) technique was utilized to explore the effect of bulk supercooling and rapid solidification in alloys with Co<sub>46</sub>Ni<sub>27</sub>Ga<sub>27</sub> and Co<sub>48</sub>Ni<sub>22</sub>Ga<sub>30</sub> (at.%) compositions. Quenching of Co<sub>48</sub>Ni<sub>22</sub>Ga<sub>30</sub> against copper led to the formation of  $\beta$  phase with grain boundaries decorated with a brittle Co-rich phase that caused deep cracks along grain boundaries. DSC experiments conducted at 10 °C/min yielded  $M_s$  and  $A_s$  temperatures of the sample at around 37.5 and 60 °C, during the first heating and cooling cycles. Slow heating/cooling at 1 °C/min suppressed the martensitic and austenitic transformation temperatures to well below room temperature. Quenched microstructure of Co<sub>46</sub>Ni<sub>27</sub>Ga<sub>27</sub>, on the other hand, consisted of  $\gamma$  dendrites surrounded by  $\beta$  ( $\beta'$ ) matrix. The presence of  $\gamma$  phase in these samples was found to suppress  $M_s$  and  $A_f$  to less than -20 and -2 °C temperatures, respectively. The Curie temperature of Co<sub>46</sub>Ni<sub>27</sub>Ga<sub>27</sub> samples remained at about 400 K regardless of the presence  $\gamma$  +  $\beta$  phases. It was shown that

**Fig. 12** Coercive forces in different directions at room temperature for  $\text{Co}_{48}\text{Ni}_{22}\text{Ga}_{30}$  (at.%) (sample D1) and  $\text{Co}_{46}\text{Ni}_{27}\text{Ga}_{27}$  samples (C2, C6, and C11)



bulk supercooling and rapid solidification can produce homogeneous single martensitic phase from the hyperperitectic  $\text{Co}_{46}\text{Ni}_{27}\text{Ga}_{27}$  alloy through partitionless solidification and/or solute entrapment. In contrast with pure martensite phase in  $\text{Co}_{48}\text{Ni}_{22}\text{Ga}_{30}$ , the off-composition martensitic phase in supercooled  $\text{Co}_{46}\text{Ni}_{27}\text{Ga}_{27}$  sample showed no grain boundaries, microsegregation and embrittlement. The sample also has a good high Curie temperature of about 400 K and good directional magnetic properties, such as different coercivity from around 14 Oe for in-plane direction to about 42 Oe at the 50° angle, and different in-plane and out-of-plane magnetizations up to saturation magnetization.

**Acknowledgements** The authors wish to thank Prof. S. Khizroev for the collaboration during evaluation of magnetic properties at the Center for Nanoscale Science and Engineering, University of California at Riverside, California 92521, USA.

## References

- Ullakko K, Huang JK, Kokorin VV, O'Handley RC (1997) Scripta Mater 36:1133
- Murray SJ, Marioni M, Allen SM, O'Handley RC, Lograsso TA (2000) Appl Phys Lett 77:886
- Wilson SA et al (2007) Mater Sci Eng R 56:1
- James RD, Wuttig M (1998) Philos Mag A 77:1273
- Kakeshita T, Takeuchi T, Fukuda T, Saburi T, Oshima R, Muto S, Kishio K (2000) Mater Trans JIM 41:882
- Chernenko VA, Cesari E, Pons J, Segui C (2000) J Mater Res 15(7):1496
- Murray SJ, Marioni MA, Kukla AM, Robinson J, O'Handley RC, Allen SM (2000) J Appl Phys 87:5774
- Albertini F, Morellon L, Algarabel PA, Ibarra MR, Paret L, Arnold Z, Calestani G (2001) J Appl Phys 89:5614
- Oikawa K, Ota T, Gejima F, Ohmori T, Kainuma R, Ishida K (2001) Mater Trans JIM 42(11):2472
- Oikawa K, Wulff L, Lijima T, Gejima F, Ohmori T, Fujita A, Fukamichi K, Kainuma R, Ishida K (2001) Appl Phys Lett 79: 3290
- Sokhey KS, Manekar M, Chattopadhyay MK, Kaul R, Roy SB, Chaddah P (2003) J Phys D Appl Phys 36:1366
- Karaca HE, Karaman I, Lagoudas DC, Maier HJ, Chumlyakov YI (2003) Scripta Mater 49:831
- Wuttig M, Li J, Craciunescu C (2001) Scripta Mater 44:2393
- Craciunescu C, Kishi Y, Lograsso TA, Wuttig M (2002) Scripta Mater 47:285
- Kishi Y, Craciunescu C, Sato M, Okazaki T, Furuya Y, Wuttig M (2003) J Magn Magn Mater 262:186
- Oikawa K, Ota T, Imano Y, Omori T, Kainuma R, Ishida K (2006) J Phase Equilibr Diffus 27:75
- Sato M, Okazaki T, Furuya Y, Wuttig M (2003) Mater Trans JIM 44:372
- Craciunescu C, Kishi Y, Graef MD, Lograsso TA, Wuttig M (2002) Proc SPIE 4699:235
- Massalski TB, Murray JL, Bennett LH, Baker H, Kacprzak L (1986) Binary Alloy Phase Diagrams. ASM
- Ducher R, Kainuma R, Ishida K (2008) J Alloys Compd 466:208
- Schlager DL, Wu YL, Zhang W, Lograsso TA (2000) J Alloys Compd 312:77
- Chernenko VA (1999) Scripta Mater 40:523
- Liu J, Xie H, Huo Y, Zheng H, Li J (2006) J Alloys Compd 420:145
- Munitz A, Abbaschian R (1986) In: Koch CC, Collings EW (eds) Undercooled alloy phases. TMS AIME, Warrendale, p 23
- Elder SP, Abbaschian GJ (1989) Principles of solidification and materials processing, vol 1. Oxford & IBH Publishing Co., p 299
- Ik Kim D, Abbaschian R (2000) J Phase Equilibr 21:25
- Ethridge EC, Curreri PA, Theiss J, Abbaschian GJ (1984) Rev Sci Instrum 55:1859
- El-Kaddah N, Szekely J (1984) Metall Trans B 15B:183
- Schlager DL, Lograsso TA, Pecharsky AO (2004) Mater Res Soc Symp Proc 785:D7.8.1
- Chernenko VA, Pons J, Cesari E, Zasimchuk IK (2004) Scripta Mater 50:225
- Liu J, Xia M, Huang Y, Zheng H, Li J (2006) J Alloys Compd 417:96
- Dantzig JA, Rappaz M (2009) Solidification. EPFL Press, Lausanne
- Abbaschian R, Kurz W (2004) In: Rappaz M, Beckermann C, Trivedi R (eds) Solidification processes and microstructures: a symposium in honor of Prof. Kurz. TMS
- Kerr HW, Kurz W (1996) Int Mater Rev 41:129
- Boettinger WJ, Coriell SR (1986) Microstructure formation in rapidly solidified alloys. In: Sahm PR, Jones H, Adam CM (eds) Science and technology of the undercooled melt. NATO ASI Series E-N0114, Martinus-Nijhoff, Dordrecht, p 81
- Aziz MJ (1996) Metall Mater Trans A 27A:671